

X-raying Abell 2125 — a Large-scale Hierarchical Complex of Galaxies and Hot Gas

Q. Daniel Wang¹, Frazer Owen², and Michael Ledlow³

ABSTRACT

We present an 82 ksec *Chandra* ACIS-I observation of a large-scale hierarchical complex, which consists of various clusters/groups of galaxies and low-surface brightness X-ray emission at $z = 0.247$. This high-resolution *Chandra* observation allows us for the first time to separate unambiguously the X-ray contributions from discrete sources and large-scale diffuse hot gas. We detect 99 X-ray sources in a $17' \times 17'$ field. Ten of these sources are identified as members of the complex and are mostly radio-bright. Whereas unresolved X-ray sources tend to be associated with galaxies in intermediate density environments, extended X-ray emission peak at bright radio galaxies in the central cluster. In particular, a distinct X-ray trail appears on one side of the fast-moving galaxy C153, clearly due to ram-pressure stripping. The diffuse X-ray emission from the central cluster can be characterized by a thermal plasma with a characteristic temperature of $3.2^{+0.5}_{-0.4}$ keV and a heavy element abundance of $0.24^{+0.15}_{-0.12}$ solar (90% confidence uncertainties). In comparison, a patch of low-surface brightness X-ray emission apparently originates in relatively low density intergalactic gas with a characteristic temperature of $0.98^{+0.22}_{-0.27}$ keV and an abundance of $\lesssim 0.09$ solar. The *Chandra* observation, together with extensive multi-wavelength data, indicates that the complex represents a projection of several galaxy sub-structures, which may be undergoing major mergers. We discuss the dynamic states of the complex and its sub-structures as well as properties of X-ray-emitting galaxies and the relationship to their environments.

Subject headings: galaxies: evolution — galaxies: general — galaxies: clusters: individual (Abell 2125) — X-rays: general — X-rays: galaxies

1. Introduction

The structure of the universe is believed to have formed by clustering hierarchically from small to large scales. The outcome of this hierarchical formation process depends largely on the interplay between galaxies and their environments. But how and where such galaxy-environment interactions primarily occur remain greatly uncertain (e.g., David et al. 1996; Wang & Ulmer 1997; Ponman et al. 1999; Fujita 2001; Balogh et al. 2002; Bekki et al. 2002).

We have identified a large-scale hierarchical complex (Fig. 1) that is well-suited for investigating the structure formation process and the environmental impact on galaxy properties. Revealed in a survey of 10 Butcher & Oemler clusters observed with the *ROSAT* PSPC (Wang & Ulmer 1997), this complex contains various X-ray-emitting features, which are associated with concentrations of optical and radio galaxies (Fig. 1; Wang, Connolly, & Brunner 1997a; Owen et al. 1999; Dwarakanath & Owen 1999). The overall optical galaxy concentration of the region was originally classified as a cluster Abell 2125 (richness 4). The *ROSAT* image and follow-up optical observations, however, have shown that the complex contains three well-defined X-ray bright clusters (Wang et al. 1997a). In addition, substantial amounts of unresolved low-surface brightness X-

¹Department of Astronomy, University of Massachusetts, Amherst, MA 01003

²National Radio Astronomy Observatory, P.O. Box 0, Socorro, NM 87801, USA

³Gemini Observatory, Southern Operations Center, AURA, Casilla 603, La Serena, Chile

ray emission (LSBXE) are also present. The overall angular size of the entire X-ray-emitting complex seems to extend more than $\sim 30'$. But the three main concentrations of galaxies (LSBXE, the central A2125 cluster, and Cluster B) are identified within a smaller projected region of dimension $\sim 12'$ ($1' = 0.23$ Mpc; the cosmological parameters, $H_0 = 71 \text{ km s}^{-1} \text{ Mpc}^{-1}$, $\Omega_{total} = 1$, and $\Omega_{\Lambda} = 0.73$ are adopted throughout the paper). The complex thus represents an X-ray-bright hierarchical filamentary superstructure, as predicted by numerical simulations of the structure formation (e.g., Cen & Ostriker 1996).

Fig. 1.— *ROSAT* PSPC X-ray image of the Abell 2125 complex and its vicinity in the 0.5–2 keV band (Wang et al. 1997a). Point-like X-ray sources detected in the image have been excised. Each contour is 50% (2σ) above its lower level. Spectroscopically confirmed, radio detected members of the complex (Owen et al. 2004a) are marked by *pluses*. The box outlines the field covered by our *Chandra* ACIS-I observation (Fig. 2). The large cross and circle show the center position and radius used in the Abell catalog.

The nomenclature adopted here (e.g., in Fig. 1) follows that used in Wang et al. (1997), based on X-ray identifications. We call the entire elongated diffuse X-ray enhancement as seen in Fig. 1 as the Abell 2125 complex. Historically, however, this congregation of optical galaxies was loosely called a cluster. The centroid listed in the Abell catalog (Abell 1958) is R.A., Dec. (J2000) = $15^h 40^m 55^s$, $66^\circ 19' 15''$, as marked in Fig. 1. The Abell radius, 9.2 (2 Mpc), encloses the bulk of the galaxy concentrations in the field of Fig. 1, including Cluster B and much of the LSBXE. The work by Butcher et al. (1983) and Butcher & Oemler (1984), however, assumed a cluster center that is close to what is inferred from the X-ray for the central Abell 2125 cluster (Fig. 1). Furthermore, their imaging field of view ($\text{FoV} = 55 \text{ arcmin}^2$) is comparable to the size of the X-ray cluster, but is much smaller than the area enclosed in the Abell radius. The central cluster itself, which is only part of the complex, is not particularly rich. This can, at least partly, explain its relatively large blue galaxy fraction ($f_b \sim 20\%$; Butcher & Oemler 1984). But, the Abell 2125 complex does seem to contain a distinct population of active galaxies (Owen et al. 2004a). There is an over-abundance of radio galaxies in Abell 2125, $\sim 9\%$ compared to a typical 2% for rich clusters at similar redshifts (Morrison &

Owen 2003).

We have obtained a deep *Chandra* observation that covers part of the Abell 2125 complex (Fig. 1) to characterize its detailed X-ray properties and to study the interplay between galaxies with their environments. The high spatial resolution of *Chandra* enables us to examine diffuse X-ray structures down to a scale of $\sim 3.8 \text{ kpc}$ ($\sim 1''$). In this paper, we concentrate on presenting the observation and the results on the detection of discrete sources and on the characterization of large-scale diffuse X-ray emission. Detailed analysis of the X-ray data in conjunction with observations in other wavelength bands will be discussed elsewhere (e.g., Owen et al. 2004a,b), although a few galaxy counterparts will be mentioned in the present work. X-ray sources are labeled with a two-digit number (with a prefix “X-” in the text), whereas optical IDs are in five-digits (e.g., 00047).

2. Observation and data Analysis

The *Chandra* observation of Abell 2125 (Obs. ID. 2207) was taken on Aug. 24, 2001 for an exposure of 81.6 ks. The instrument ACIS-I was at the focal plane of the telescope and in the “VERY FAINT” mode. Our data calibration follows the same procedure detailed by Wang et al. (2004). Briefly, we reprocessed the level 1 (raw) event data to generate a new level 2 event file, using the *Chandra* Interactive Analysis of Observations software package (CIAO; version 2.3). The re-processing includes an improved absolute astrometry of the observation (nominally better than $\sim 0.3''$), a correction for the charge transfer inefficiency of the CCDs, and a better software rejection of particle-induced events (i.e., setting the flag `check_vf_pha=yes` when running the CIAO program `acis_process_events`). We further removed time intervals with significant background flares, or peaks with count rates $\gtrsim 3\sigma$ and/or a factor of $\gtrsim 1.2$ off the mean background level of the observation, using Maxim Markevitch’s light-curve cleaning routine “lc_clean”. This cleaning, together with a correction for the dead time of the observation, resulted in a net 80.5 ks exposure (livetime) for subsequent analysis.

We constructed broad band X-ray intensity images by flat-fielding count images with corresponding effective exposure maps, weighted with

Fig. 2.— *Chandra* ACIS-I images of the Abell 2125 field in the 0.5-2 keV (upper panel) and 2-8 keV (lower panel) bands. The images are smoothed with a Gaussian of FWHM equal to $3''$. The small circles represent the regions removed for discrete sources, which are labeled as in Table 1. The two large circles represent the cluster and the LSBXE, while the large ellipse outlines the diffuse emission to the southwest. The two squares outline the off-source background regions, from which spectra are extracted.

a power law of photon index 1.7. This flat-fielding corrected for telescope vignetting and bad pixels as well as the quantum efficiency variation of the instrument, including an observing date-dependent sensitivity degradation, which is particularly important at low energies $\lesssim 1.5$ keV.

We searched for X-ray sources in the three broad bands, (S) 0.5-2, (H) 2-8, and (B) 0.5-8 keV. In each band, we successively applied the source detection and analysis algorithms: wavelet, sliding-box, and maximum likelihood centroid fitting; the procedure for these applications as well as the related background map construction was detailed by Wang et al. (2003). The significance of a source detection is characterized by the false detection probability P due to a random background fluctuation:

$$P = 1 - \sum_{n=0}^{n_c-1} \frac{n_b^n}{n!} e^{-n_b}, \quad (1)$$

where n_c and n_b are the total numbers of counts, detected and expected from the local diffuse background. The above definition of P is slightly different from that used in Wang et al. (2003), where the upper limit of the summation in equation (1) was set to be n_c . When $P < 10^{-6}$ (our chosen threshold), a positive source detection was claimed. Source count rates were estimated within the 90% energy-encircled radius (EER) of the point spread function (PSF), which is off-axis dependent (Fig. 2; Jerius et al. 2000). The calculation of the EER assumed a mean X-ray spectrum as a power law with a photon index equal to 1.7, typical for an AGN. But individual sources could have very different spectra. To minimize the dependence on the assumed spectrum, the correction was made individually in each of the four narrower bands (0.5-1, 1-2, 2-4, and 4-8 keV), before the source count rates were combined into the above broad bands. The spectral variation also introduce uncertainties in our estimate of the detection threshold. This explains why a couple of sources have count rates below the thresholds in Fig. 3.

To determine how many of our detected sources may be associated with the A2125 complex, we need to estimate the number of possible interlopers (e.g., background AGNs). We use the $\text{Log}(N)$ – $\text{log}(S)$ relation presented by Moretti et al. (2003 and references therein) for sources detected separately in the 0.5-2 keV and 2-10 keV bands, assuming a power law of photon index of 1.4 and a foreground absorption column density $N_H = 1.6 \times 10^{20} \text{ cm}^{-2}$. To convert the flux S back into the ACIS-I count rate, we assume the same power law and $N_H = 3 \times 10^{20} \text{ cm}^{-2}$, appropriate for our field. The corresponding conversion is 0.45 and $3.0 \times 10^{-11} \text{ (erg cm}^{-2} \text{ s}^{-1})/(\text{counts s}^{-1})$ in the 0.5-2 keV and 2-10 keV bands, respectively.

The sensitivity of our source detection depends on the size of the PSF as well as the local background level and effective exposure, which all vary with position, especially with the off-axis angle (Fig. 3). This variation can seriously affect the number-flux distribution of the detected sources, except for those with count rates $\gtrsim 5 \times 10^{-4} \text{ counts s}^{-1}$ (Fig. 3). Furthermore, because of the limited counting statistics, many sources have very uncertain count rates. As a result of this large uncertainty, together with a typical steep number-flux distribution of background sources, more faint sources are expected to be scattered to fluxes above the detection limit than the other way around. This is similar to the Eddington bias in optical photometry (Hogg & Turner 1998) and is accounted for in our calculation of the expected interlopers in the field, according to the procedure detailed in Wang (2004).

We removed a region of twice the 90% 0.5-8 keV band EER around each source to study diffuse X-ray emission (Fig. 2). For visual presentation of smoothed diffuse X-ray intensity maps, we replaced the source-removed region with values estimated from data in surrounding bins.

In our diffuse X-ray spectral analysis, we take special care of the background subtraction. We estimated the background contribution in off-source

regions (Fig. 2). To check the consistency of the background spectral properties in different regions, we compared the on- and off-source spectra extracted from the so-called blank-sky data¹. With an effective livetime of 550 ks, the data were re-projected to mimic our observation, accounting approximately for both the cosmic X-ray background and the contribution from charged particle-induced events. We found that a simple re-normalization of the off-source spectrum yielded statistically consistent on- and off-source blank-sky spectra. The re-normalization corresponded to a reduction of the livetime of the off-cluster spectrum by a factor of 1.16 ($\chi^2/d.o.f. = 360.7/328$). The renormalized off-source background of our observation was then used for the background subtraction in spectral analysis within XSPEC (Arnaud 1996). For the LSBXE feature, the on- and off-source blank-sky spectra, are statistically consistent with each other ($\chi^2/d.o.f. = 482.5/450$). The best-fit normalization factor is 1.02, resulting only marginal improvement of the fit ($\chi^2/d.o.f. = 472.5/450$). We therefore, used the off-source spectrum from our observation without the normalization for the background subtraction of the LSBXE spectral analysis. Similarly, no background intensity normalization is needed for the southwest diffuse feature (Fig. 2; the southwest hereafter; §3.2)

3. Results

3.1. Discrete X-ray Sources

Fig. 2 presents an overview of the ACIS-I image and the detected X-ray sources, which are listed in Table 1. Various parameters are defined in the note to the table. The conversion from a count rate to an absorption-corrected energy flux depends on the source spectrum (Fig. 4). The hardness ratios, compared with the models (Fig. 5) may be used to characterize the X-ray spectral properties of relatively bright sources. A typical value of the conversion is $\sim 8 \times 10^{-12}$ (erg cm⁻² s⁻¹)/(counts s⁻¹) in the 0.5-8 keV band, appropriate for a power law spectrum of photon index 2 and an absorbing-gas column density $N_H \sim 1 \times 10^{21}$ cm⁻². This conversion should be a good approximation (within a factor of 2) for

$\lesssim 3 \times 10^{21}$ cm⁻² (Fig. 4). The corresponding conversion to a source-frame luminosity in the same band is $\sim 1.4 \times 10^{45}$ (erg s⁻¹)/(counts s⁻¹) at the distance of Abell 2125. One can then estimate from the observed count rate the star formation rate as $\sim 6.8 \times 10^{-41} L_{2-8\text{keV}} M_\odot \text{ yr}^{-1}$ for starburst dominant galaxies (Ranalli, Comastri, & Setti 2003; Owen et al. 2004a).

Most of the sources are detected in multiple bands, including 81 and 48 detections in the 0.5 - 2 keV and 2 - 8 keV bands, respectively. In comparison, the expected numbers of interlopers are 75 and 45 in the same two bands. Ten of the sources (Table 1) are in positional coincidence with member galaxies of the A2125 complex (Owen et al. 2004a). While one of the member sources (X-65) has a count rate of 1.8×10^{-3} counts s⁻¹, all others have count rates $\sim 2.4 - 7.4 \times 10^{-4}$ counts s⁻¹, in which there is an excess of the observed number-flux (count rate) distribution of sources above the predicted interloper contribution. With these member sources excluded, which are all detected in the 0.5-2 keV band, the observed and predicted distributions are consistent with each other (Fig. 6). This direct comparison (without a fit) gives $\chi^2 = 9.9$ for 9 bins compared with $\chi^2 = 20.5$ for 10 bins without the exclusion of the member sources. Therefore, the total excess above the expected number of interlopers is at ~ 2 confidence level, but few (if any) of the remaining unidentified sources are likely to be members of the complex.

3.2. Diffuse X-ray Emission

We present in Fig. 7 adaptively smoothed ACIS-I intensity images. The presence of the large-scale diffuse X-ray emission is apparent. The overall morphology of the diffuse emission is very similar to that seen in Fig. 1, although part of the PSPC counts is clearly due to point-like sources detected now in the ACIS-I image. The diffuse emission is substantially softer than typical discrete sources. There are substructures in the diffuse X-ray emission on all scales, which may be more easily appreciated in images that are less heavily smoothed (e.g., Fig. 8).

Let us first discuss the relatively small-scale, but quite conspicuous, diffuse X-ray feature, the southwest (Figs. 2, 7, and 8). Fig. 9 shows a close-up of the field, which also contains three discrete sources (Table 1; Fig. 2). X-17 is identified with

¹available at <http://cxc.harvard.edu/contrib/maxim/acisbg/data/README>

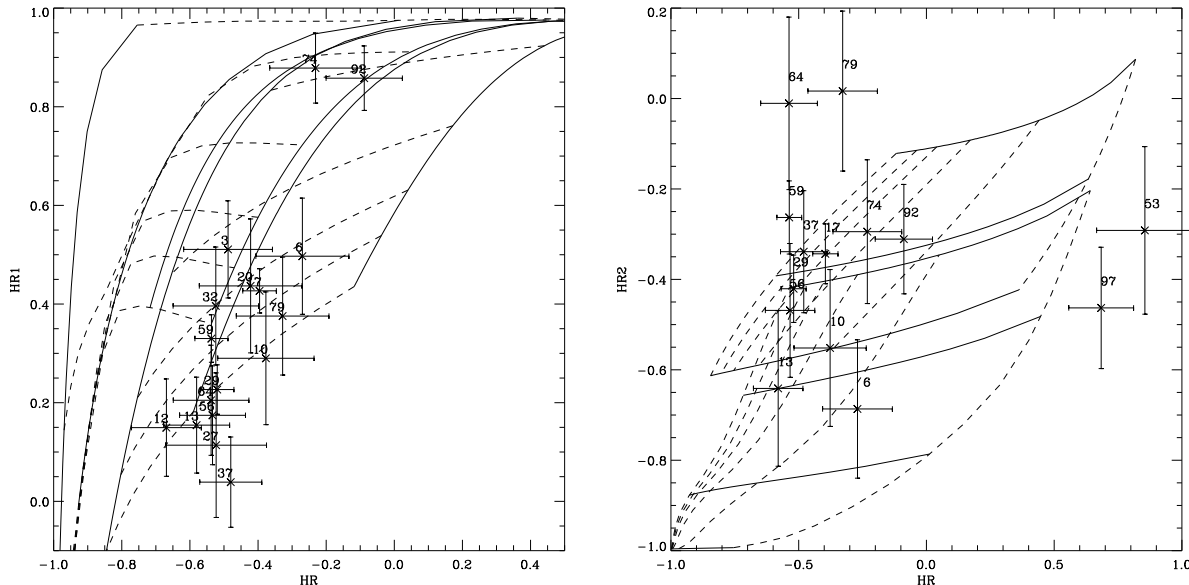


Fig. 5.— Color-color diagrams of X-ray sources with their generic numbers (Table 2) labeled. The hardness ratios (HR1, HR2, and HR) are defined in the notes to Table 1, and the error bars represent 1σ uncertainties. Also included in the plot are hardness-ratio models: the solid thick curves are for the power-law model with photon index equal to 3, 2, and 1, whereas the solid thin curves are for the thermal plasma with a temperature equal to 0.3, 1, 2, and 4 keV, from left to right in the left panel and from bottom to top in the right panel, respectively. The absorbing gas column densities are 1, 10, 20, 40, 100, and $300 \times 10^{20} \text{ cm}^{-2}$ (dashed curves from bottom to top in the left panel and from left to right in the right panel)

Fig. 8.— ACIS-I diffuse X-ray intensity images in three bands: 0.5-1 keV (a), 1-2 keV (b), and 2-8 keV (c). The images are adaptively smoothed with a Gaussian, the size of which is adjusted to achieve a uniform count-to-noise ratio of ~ 6 across the field. Removed sources are marked with crosses, whereas regions of the large prominent diffuse features are labeled in (a)

a galaxy, which our optical spectroscopy shows to be at $z=0.29$ (Miller et al. 2004). The other two sources (X-9 and X-11) also appear to have optical counterparts, albeit very faint. These discrete X-ray sources all have hard spectral characteristics, as evidenced by their relative high fluxes in the 2-8 keV band (Fig. 7a). In comparison, the extended X-ray feature has a substantially softer spectrum (Fig. 10; §2), with the emission primarily in the 0.5-2 keV band.

What might be the nature of the southwest? Located at a large off-axis angle in the ACIS-I image, the feature could be a combination of several physically-unrelated components. The X-ray counting statistics of the feature (~ 540 counts) is also not sufficient for a detailed spectral analysis. Nevertheless, we have attempted a simple spectral characterization of the feature, by fixing the absorption to be the Galactic foreground

($N_H \sim 3 \times 10^{20} \text{ cm}^{-2}$). A spectral fit with a thermal plasma model then suggests that the feature may represent a cluster at $z \sim 1$ (Fig. 10). The temperature 3.1(2.3-4.1) and the inferred 0.5- 8 keV luminosity $\sim 1.4 \times 10^{44} \text{ erg s}^{-1}$ (in the rest frame of the putative cluster) are consistent with the normal correlation between the two parameters expected for clusters (Wu, Xue, & Fang 1999, corrected for our adopted Hubble constant). The small size of the feature also agrees with this interpretation. But, the best-fit metal abundance seems to be unusually high (greater than the solar; the upper limit is not constrained), mainly due to two apparent emission line features at ~ 1.0 (SiIV) and 1.2 (SXV-SXIV). Furthermore, the X-ray feature is apparently associated with an excess of very faint galaxies (Fig. 9), again consistent with the distant cluster interpretation. Clearly, more observations are required to establish the

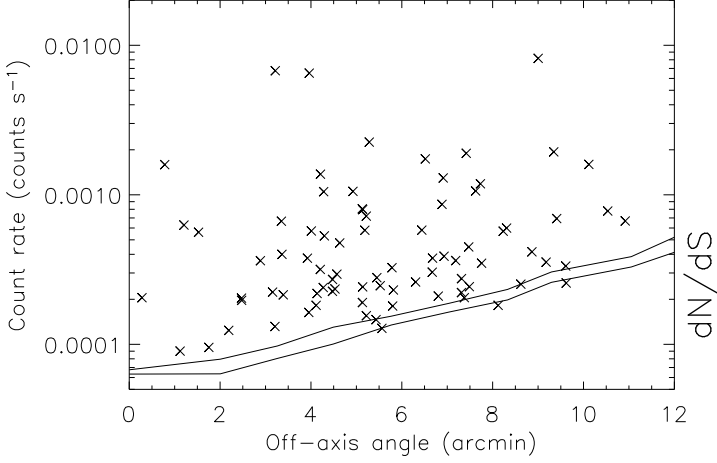


Fig. 3.— Count rates of sources detected in the 0.2-5 keV band vs. the off-axis angle of the ACIS-I observation. The upper and lower curves illustrate the approximate 0.2-5 keV band detection thresholds, the azimuthally averaged and the lowest at each off-axis angle, respectively.

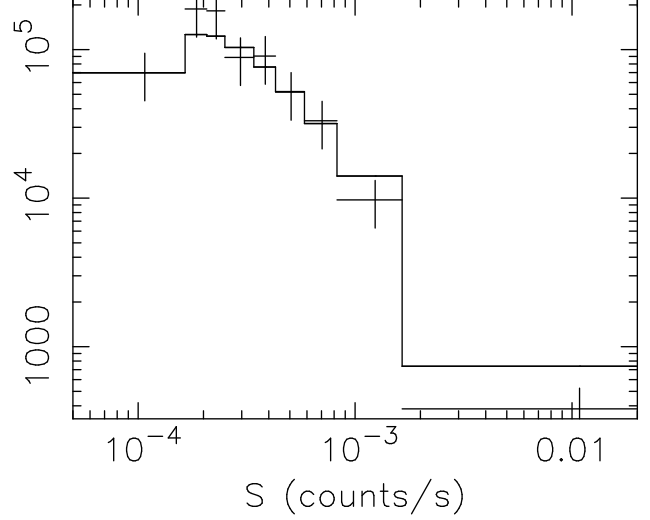


Fig. 6.— The source count rate distribution of detected X-ray sources, excluding known complex members, compared with the expected background contribution (histogram) in the 0.2-2 keV band.

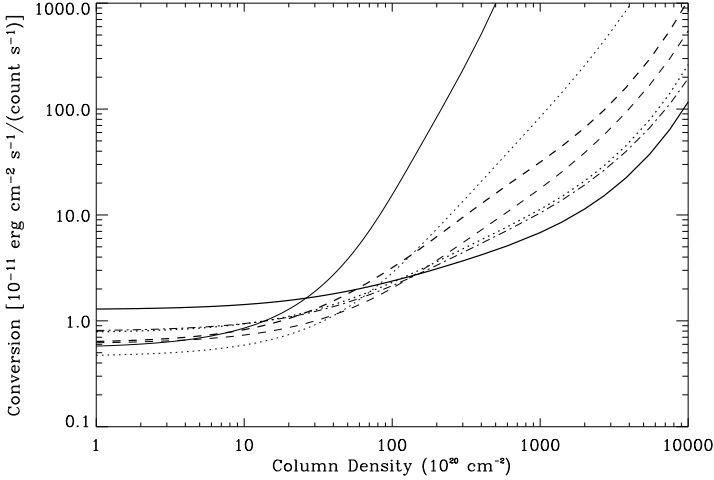


Fig. 4.— Conversion of an ACIS-I count rate to an energy flux in the 0.5-8 keV band for representative models: the thick curves are for the power-law model with a photon index equal to 1 (solid), 2 (dotted), and 3 (dashed), whereas the thin curves are for the thermal plasma with a temperature equal to 0.3 (solid), 1 (dotted), 2 (dashed), and 4 (dot-dashed) keV, respectively. The heavy element abundance is assumed to be solar for both the X-ray-emitting plasma and the absorbing gas.

Fig. 7.— ACIS-I intensity images of the Abell 2125 complex: (a) a tri-color montage of X-ray intensities in the 0.5-2 keV (red), 2-4 keV (green), and 4-8 keV (blue) bands; (b) the 0.5-2 keV band only with green squares mark the positions of complex member galaxies (radio- and X-ray-bright ones are further marked in blue and with crosses); (c) the core of the Abell 2125 cluster (2′36×2′36 FoV) in the Kitt Peak 4-m mosaic V-band (red) as well as in the 0.5 - 2 keV (green) and 2 - 8 keV (blue) bands; (d) a close-up of C153 (00047) in an *HST* WFPC-2 V-band (red; Owen et al. 2004b) and its diffuse X-ray trail (the same color-code as in the panel c; 0′426 × 0′491 FoV).

true nature of the X-ray feature. We will not discuss it further in the present work.

The remaining diffuse X-ray emission is correlated well with identified complex member galaxies (e.g., Fig. 7b). Two relatively prominent concentrations are sampled by the ACIS-I observation: the Abell 2125 cluster and the southwest LSBXE patch. The X-ray spectra of these two diffuse X-ray features are presented in Fig. 11. The total number of counts included in the spectral fits (Fig. 11) is 5627 for the cluster and 1819 for the LSBXE, including about 1450 and 790 background counts within the respective circular regions defined in Fig. 2. The spectra are grouped to achieve a net (background-subtracted) signal-to-noise ratio greater than 3 in each bin. The results of the spectral fits are summarized in Table 2. We have obtained these results by assuming the mean optical redshift of the complex to be $z = 0.247$, which is consistent with our direct fit to the X-ray spectral data: $z = 0.23(0.21 - 0.25)$ for Abell 2125 and $0.30(0.06 - 0.5)$ for the LSBXE (all uncertainty ranges are at the 90% confidence level). The results are not sensitive to the exact aperture used for the spectral extraction (Fig. 2).

The diffuse X-ray surface brightness intensity of a relaxed cluster can typically be characterized by the standard β -model of the form (Cavaliere & Fusco-Femiano 1976):

$$I = I_o \left(1 + \frac{r^2}{r_c^2} \right)^{1/2-3\beta}, \quad (2)$$

where r is the off-center radius. However, the model gives a poor fit to the azimuthally-averaged radial surface brightness intensity distribution in the 0.5-8 keV band ($\chi^2/d.o.f. = 107/56$) and can be rejected at a confidence of $\sim 5\sigma$.

The morphology of the cluster is far from the axis-symmetric. We characterize the morphological variation of the cluster with a series of ellipses on various scales (Fig. 12). Each ellipse is determined by the moments of the enclosed X-ray intensity distribution (e.g., Carter & Metcalfe 1980;

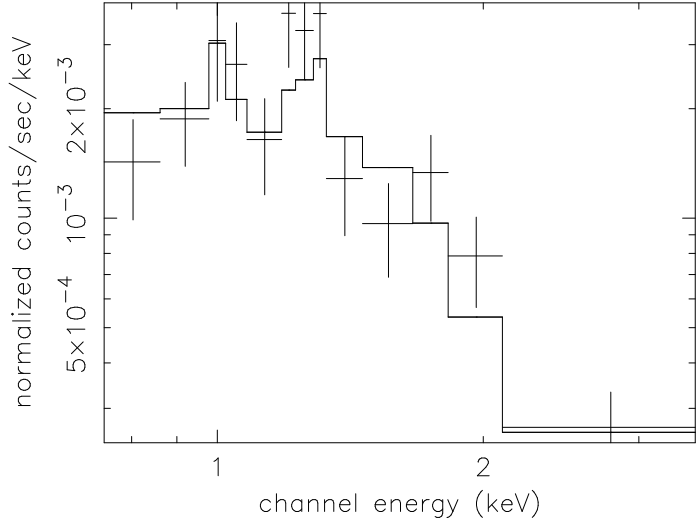


Fig. 10.— ACIS-I Spectra of the southwest, together with the best-fit thermal plasma spectra model (see text for details). The on-source spectral data were extracted from the ellipse outlined in Fig. 2 (see also §2).

Fig. 9.— Overlay of ACIS-I intensity contours on a Kitt Peak 4-m R-band image of the southwest (see also Fig. 2). The X-ray intensity is smoothed in the same way as in Fig. 7. The contour levels are at 3.6, 3.9, 4.5, 5.4, 6.6, 8.1, 10, 18, 33, and 63×10^{-3} counts s^{-1} arcmin $^{-2}$.

Fig. 12.— Characterization of the 2-D morphology of the 0.5-8 keV diffuse emission from the Abell 2125 cluster with ellipses on evenly-spaced scales from 0'.5 - 2'.5. The gray-scale map is in the 0.5-2 keV band and is adaptively smoothed with a count-to-noise ratio of 6.

Fig. 11.— ACIS-I Spectra of the Abell 2125 cluster (left panel) and the LSBXE (right panel), together with the best-fit spectra models (Table 2).

Wang, Ulmer, & Lavery 1997b). We follow the iterative approach detailed in Wang et al. (1997b) to calculate the four parameters that define an ellipse: the center coordinates (R.A. and Dec. shifts relative to the aiming direction of the ACIS-I observation), ellipticity (ϵ), and orientation of the major axis (θ ; north to east). The results obtained from the 0.5-8 keV band data are presented in Figs. 12 and 13. Note that the 90% statistical confidence error bars on different scales are not totally independent and thus overestimated, as the calculation of the moments uses all the data with each ellipse (Wang et al. 1997b). The most significant change of the ellipse parameters with the semi-major axis is the center R.A. position, which shifts by $\sim 10''$ from the inner region to outer region of cluster. The centroid of the cluster is offset to the northwest from the central triple of major cD-like galaxies (Fig. 7c). This offset as well as the centroid shift and the elongation of the cluster morphology may be a manifestation of the underlying gravitational mass distribution. Galaxies in the field show another concentration about $1'.4$ to the northwest (Fig. 7c). But the diffuse X-ray emission extends further to the north on larger scales (Fig. 12). This extension is reflected in the change of the ellipse orientation with the scale

(Fig. 13, lower right panel).

Ignoring these small, though significant, morphological variations, we use the elliptical coordinates as defined by the ellipse parameters on the $2'.5$ scale (Table 3) to measure the surface brightness intensity profile as a function of the semi-major axis. A β -model fit to this profile obtained in the elliptical coordinates is acceptable (Fig. 14; Table 3) and may thus be considered as a characterization of the average large-scale properties of the cluster. We infer from the model the central electron density as $n_0 \sim 2.0 \times 10^{-3} \text{ cm}^{-3}$, assuming an oblate shape of the X-ray-emitting medium and the best-fit thermal plasma model (Table 2). The mean cooling time scale of the gas at the center of the cluster is then $\sim 18 \text{ Gyr}$, which is longer than the age of the Universe.

We have also conducted the same morphological characterization of the cluster in the 0.5-2 keV band. The 2-D ellipse fit in this band gives the ellipse parameters that are nearly identical to those in the 0.5-8 keV band, especially on the $2'.5$ scale. Except for the central intensity $I(0)$, the best-fit β -model parameters in the two bands are statistically consistent with each other, particularly with the consideration that β correlates with the core radius r_c in the parameter estimation. But the

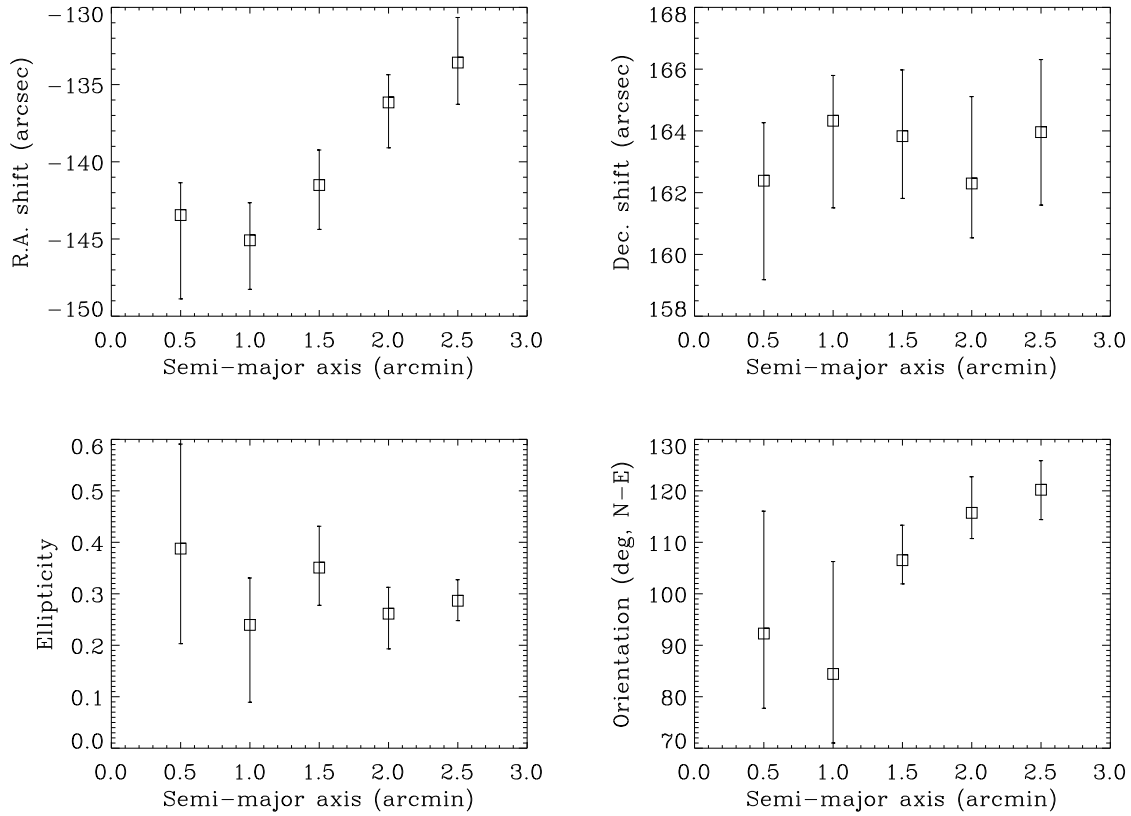


Fig. 13.— Center shifts, ellipticity, and orientation of the 0.5-8 keV intensity isophote ellipse as a function of semi-major axis of the Abell 2125 cluster. Error bars are at the 90% confidence level.

fit is much less satisfactory in the 0.5-2 keV band than in the 0.5-8 keV band.

3.3. X-ray Substructure in the Central Cluster

A careful inspection of the cluster images in various bands indicates that much of the deviation of the X-ray intensity distribution from the global elliptical β -model is caused by the presence of small-scale substructures, which are particularly apparent in the 0.5-2 keV band. For example, Figs. 7c,d clearly show energy-dependent features, which are strikingly associated with several massive radio galaxies in the cluster. Comparison with point-like sources in the vicinity indicates that these peaks are resolved. Their shapes in the figures are, however, affected by the overall X-ray intensity gradient across the cluster. To minimize this effect, we subtract the best-fit elliptical β -model from the 0.5-2 keV intensity map. Fig. 15 compares the X-ray intensity residuals and the radio contours. The enhanced soft X-ray peaks are clearly associated with the galaxies 00047 ($z=0.2528$) and 00057 ($z=0.2518$), although only the former is detected as a discrete source (Table 1).

The most outstanding feature in this residual image is a “trail” (X-68) apparently attached to the optical galaxy 00047, which has a radio counterpart C153 (Owen et al. 2004a; Fig. 15; see also Figs. 7c,d). This trail is only apparent in the 0.5-2 keV band and extends about $22''$ (corresponding to ~ 88 kpc at the distance of the cluster) from the galaxy to the northeast. A similar, though shorter, trail in the same direction is also seen in [OII] line emission (Owen et al. 2004b). With the limited counting statistics of the data, however, we cannot conclude that this apparent trail indeed represents a coherent diffuse X-ray structure. While the association of the first $\sim 10''$ high surface brightness portion of the trail with the galaxy is convincing, the rest may become mixed up with other things, including possible weak discrete sources and/or statistical fluctuations. Fig. 16 compares the surface brightness intensity across the trail. From this comparison, we estimate the average width of the trail as $\sim 4''$ (~ 16 kpc) and the total net count rate above the local background of ~ 0.01 counts s^{-1} arcmin $^{-2}$ as $\sim 5.3(\pm 0.9) \times 10^{-4}$ counts s^{-1} in the 0.5-1.5 keV band.

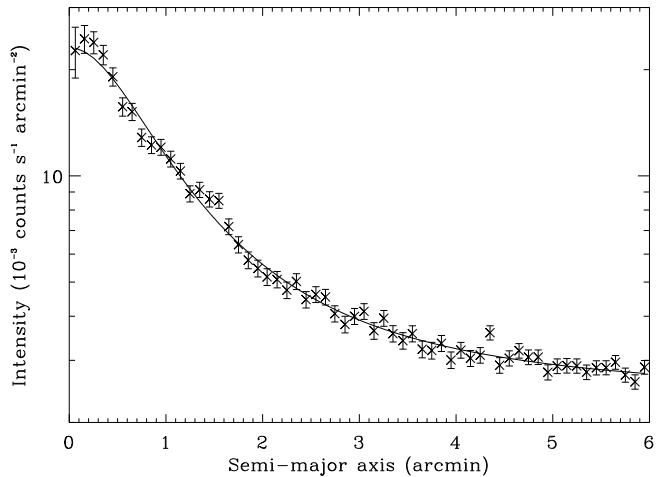


Fig. 14.— ACIS-I 0.5-8 keV surface brightness profile of Abell 2125 in the elliptical coordinates defined by the best-fit isophote ellipse on the scale of $5'$ semi-major axis. The curve represents the best-fit β -model.

Fig. 15.— Residual map of the ACIS-I intensity in the core of the Abell 2125 cluster, after subtracting the best-fit elliptical β -model (Fig. 14; Table 3). The image is smoothed with a Gaussian of FWHM equal to $6''$. The overlaid 20-cm continuum intensity contours are at 0.04, 0.08, 0.16, 0.32, 0.64, 0.96, 2, 4, and 8 mJy/beam (Dwarakanath & Owen 1999). The large thick *plus* sign marks the adopted global cluster center (Table 3), while the *crosses* show the locations of the optical positions of the four radio galaxies: 00047, 00057, 00105, and 00106 from right to left (Owen et al. 2004b).

4. Discussion

The above results provide a detailed characterization of the diffuse X-ray emission and discrete sources in the Abell 2125 complex. In the following, we try to address several key issues about the complex by incorporating the results with information learned from observations in other wavelength bands.

4.1. Abell 2125 as a Large-scale Hierarchical Complex

This distinct complex of galaxies and hot gas shows several remarkable characteristics:

- a large velocity dispersion which appears to be due to two or three major components with a total projected extent of several Mpc (Miller et al 2004);
- an exceptionally large fraction of radio galaxies, which are located primarily outside the central Abell 2125 cluster (Owen et al. 2004a);
- the presence of multiple X-ray-emitting clusters and LSBXE features, each with substantially lower luminosity and temperature than expected from the overall galaxy richness and large velocity dispersion of the complex (see also Wang et al. 1997).

Comparisons with various numerical simulations indicate that the complex represents a projection of multiple components, which might be in a process of merging with each other (Miller et al. 2004; Owen et al. 2004a). Projection effects, together with enhanced activities during this process, may explain the observed characteristics.

4.2. Nature of the LSBXE

Globally speaking, the prominent southwest patch of the LSBXE characterized here probably represents a local temperature and density enhancement of a large-scale diffuse intergalactic medium (IGM) structure, as indicated first in the *ROSAT* PSPC image (Fig. 1), which is more sensitive to very soft X-rays ($\lesssim 0.5$ keV) than the *Chandra* observation.

The LSBXE is distinctly different from the central cluster. Even the relatively X-ray-bright

southwest patch does not seem to be centrally peaked, as may be expected from a more-or-less virialized intracluster medium (ICM). The kinematics (Miller et al. 2004) indicates that the galaxies in this patch are probably loosely bound, although their exact line-of-sight distribution is not clear. Figs. 17c,d show a sub-field of the LSBXE, as sampled by an *HST* WFPC-2 image. X-14 and X-22 may be associated with two bright ellipticals in the field. But the centroid of X-14 is closer to a faint point-like optical object about $4''$ offset from the corresponding elliptical. Therefore, the X-ray source may represent a background AGN. Most of other galaxies in the field appear to be spirals. X-ray emission from such galaxies are typically dominated by X-ray binaries and/or AGNs and is therefore expected to have a relatively hard spectrum. But the diffuse X-ray enhancement associated with the galaxy concentration is soft, indicating an origin in diffuse hot gas around individual galaxies, in groups of galaxies, and/or in the intergroup IGM.

The heavy element abundance in the LSBXE appears to be substantially lower than that in the ICM of the central cluster. The abundance may be underestimated in the LSBXE, if it contains multiple temperature components. Although the single temperature thermal plasma gives a satisfactory fit, we also tried a model with two temperature components. This model gives a marginally improved fit to the LSBXE spectrum ($\chi^2/d.o.f = 18.2/23$, compared with that in Table 2), but provides no useful constraints on the abundance, because of the limited counting statistics of the data. If the low metallicity obtained from the single temperature plasma fit is real, there may be two possible explanations: 1) Metals (mainly irons) are largely locked in dust grains within or around galaxy groups (e.g., Nollenberg, Williams, & Maddox, 2003); 2) The metals are still bounded by individual galaxies (e.g., Tsai & Mathews 1996). Dust grains may survive, and may even not mix well with, the X-ray-emitting gas in a quiescent, low density environment. But the mixing should likely to occur during or after the merger of a galaxy or group with a cluster. The dust grains would then be destroyed rapidly by sputtering in the ICM of high density and temperature. This may explain the metal abundance difference in the X-ray-emitting gas between the

LSBXE and the central cluster.

4.3. Dynamical State of the Central Cluster

This central cluster (Abell 2125; Fig. 1) represents the strongest enhancement of the diffuse X-ray emission in the complex. The relative values of our measured temperature and luminosity of the ICM (Table 2) are consistent with those for typical clusters (e.g., Wu et al. 1999). From the mass-temperature relationship (e.g., Shimizu et al. 2003), we may then expect the virial mass of the cluster as $2 - 5 \times 10^{14} M_{\odot}$. For a virialized system, the temperature would also predict a galaxy velocity dispersion of $\sim 6.5 \times 10^2 \text{ km s}^{-1}$. This velocity dispersion is considerably smaller than $\sim 8.3 \times 10^2 \text{ km s}^{-1}$ (assuming to be isotropic), inferred from the radial velocity dispersion of $\sim 4.8 \times 10^2 \text{ km s}^{-1}$ estimated from the modeling of the velocity field (Miller et al. 2004). Interestingly, the two brightest compact radio galaxies, 00047 and 00057, are moving at high velocities ($\sim 1.5 - 1.8 \times 10^3 \text{ km s}^{-1}$) relative the mean of the cluster. It is conceivable that these two galaxies might simply represent a background cluster/group projected in the same sky by chance. The projected closeness of the galaxies to the center of the cluster and their enhanced diffuse X-ray emission, however, suggest that the association is physical, consistent with that the cluster is experiencing a major merger probably in a direction close to the line of sight. Indeed, 00047 is a strongly disturbed disk-like galaxy and the associated diffuse X-ray emission forms a trail, as expected from a ram-pressure stripping. 00057 and other two radio galaxies in the core of the cluster are all cD-like ellipticals (Figs. 7c and 15).

Furthermore, the 2-D morphology of the cluster in the sky, as shown in §3.2, also suggests that it is far from a relaxed system. The X-ray morphology is strongly elongated and shows the centroid shift with scales, strongly indicating an ongoing merger (e.g., Roettiger et al. 1993). The measured X-ray ellipticity of the cluster is the largest in the Butcher & Oemler sample (Wang & Ulmer 1997). The X-ray centroid is further offset from the cD galaxies in the cluster core (Fig. 15). A northwest-southeast elongation is also seen in the galaxy distribution, similar to the X-ray morphology (Owen et al 2004b). One separate sub-cluster, at least,

can be found in the NW extension of the cluster and is centered on a radio-loud cD-like galaxy (00039) and coincides with the bright soft X-ray source X-65 (Fig. 17a). This galaxy has a similar optical magnitude as those three cDs in the core. Furthermore, the velocity of the galaxy is comparable to those of the north and northeast cDs in the core, suggesting that the merger axis is nearly perpendicular to the line of sight. This northwest-southeast sub-cluster merger provides a natural explanation for the wide-angle tailed radio source attached to one (00106) of the two low-velocity ellipticals in the cluster core (Fig. 15), which suggests a pressure gradient or relative motion of the local gas in the plane of the sky. In short, the central cluster is undergoing a merger, possibly in multiple directions. As clusters are expected to be found at intersections of cosmic webs, such a complicated merger process is probably common for clusters still in early formation stages.

What might be the relationship between the LSBXE and the central cluster? The velocity centroids of the associated galaxy concentrations appear to be comparable (Miller et al. 2004). Spatially, the two concentrations are separated by $\sim 7'$, or a projected distance $d_p \sim 1.6 \text{ Mpc}$. One possibility is that the cluster and the LSBXE are merging in the plane of the sky. There are galaxies occupying the area between the LSBXE and the central cluster with the similar velocity (as well as a separate higher velocity component; Miller et al. 2004). There is also faint diffuse X-ray emission in the area, although the quality of the data does not allow for a distinction between a projection effect and a true dynamical interaction between these two concentrations. Alternatively, the two concentrations may be physically separated by a turn-around distance d_t so that their relative velocity is near zero. Following Sarazin (2003), we estimated $d_t \approx 2(GM)^{1/3}(t_t/\pi)^{2/3} \approx (7 \text{ Mpc})(M/10^{15} M_{\odot})^{1/3}(t_t/10^{10} \text{ yr})^{2/3}$, where M is the total gravitational mass of the two concentrations, and t_t is the age of the Universe at the turn-around time. If the system starts to collapse for the first time at $z = 0.247$, the axis is then oriented relative to the line of sight by an angle $\sim \sin^{-1}(d_p/d_t) \sim 16^\circ$ for $M \sim 5 \times 10^{14} M_{\odot}$ (see above). If the two concentrations have already passed across each other (i.e., the first collapse occurred much earlier) and is about to re-collapse,

the angle would then be larger.

4.4. Galaxy-Environment Interaction

As marked in Table 1 and Fig. 7b, 10 X-ray sources are identified as member galaxies of the Abell 2125 complex. Eight of them are radio galaxies, preferentially in the LSBXE region. Most of these X-ray-loud galaxies are not resolved by *Chandra* and are probably dominated by AGN activities. Two of the X-ray sources are apparently resolved and are associated with the giant elliptical galaxy 00039 and the disturbed disk-like galaxy 00047 (C153) in the central Abell 2125 cluster (Figs. 15 and 17a,b). As our source detection algorithms are optimized to detect point-like sources, extended sources such as the one associated with 00057 (Fig. 15) is not listed in Table 1. These extended soft X-ray enhancements probably represent hot gas associated with individual massive galaxies or groups of galaxies, which may have entered the cluster for the first time. Outside the central cluster, the ambient density and relative velocity are typically low and the ram-pressure stripping is probably not important, at least for massive galaxies. The intergalactic gas around galaxies may even cool fast enough to replenish the gas consumed for star formation (Bekki et al. 2002). As they are plugging into a cluster, the surrounding gas may then be compressed by the high ram-pressure of the ICM, resulting in enhanced soft X-ray emission. The eventual stripping of the gas and dust may be important in both enriching the ICM and transforming the galaxies (e.g., Bekki et al. 2002).

C153 represents an extreme case of the ram-pressure stripping. This galaxy probably went through the cluster central region quite recently (Fig. 15). The absence of the trail above 1.5 keV (Fig. 15) suggests that the gas in the trail is substantially cooler ($kT \lesssim 1.5$ keV) than the ambient ICM, assuming collisional ionization equilibrium. (The the gas, if heated from a cool phase, may well be out of the equilibrium.) The emissivity of the hot gas in the ACIS-I 0.5-1.5 keV band (Fig. 15) peaks at $kT \sim 0.7$ keV, but is within a factor of 2 as long as $kT \gtrsim 0.35$ keV. We estimate the luminosity of the trail as $\sim 5 \times 10^{41}$ ergs s⁻¹ in the 0.5-2 keV band, which only weakly depends on the assumed gas temperature. To proceed further, we assume that the entire trail can be ap-

proximated as a uniform cylinder of ~ 88 kpc long and 16 kpc diameter (Figs. 15-16; §3.3). The mean electron density can then be estimated as $\sim 1.0 \times 10^{-2} \text{ cm}^{-3} \xi^{-0.5}$, where ξ is the gas metallicity in the solar units. The dependence on ξ assumes that metal lines dominate the X-ray emission. If the X-ray-emitting gas in the trail is roughly in a pressure balance with the ICM ($p/k \sim 7.7 \times 10^4 \text{ cm}^{-3} \text{ K}$; §3.2), the required gas temperature is then $kT \sim 0.6 \text{ keV} \xi^{0.5}$. We further estimate the total mass and radiative cooling time scale of the gas in the trail as $\sim 5 \times 10^9 \xi^{-0.5} M_\odot$ and ~ 1 Gyr. If the gas is far from uniform in the trail, however, the cooling time could then be much shorter and may be compared to the crossing time scale of the galaxy through the cluster (a few times 10^8 years).

A more thorough multiwavelength investigation of galaxy properties and their relationship to the local and global environment will be presented by Owen et al. (2004a,b). In particular, our X-ray source detection reported here is optimized for point-like sources and the detection threshold is quite conservative, which minimizes the global probability of including spurious sources in our list. With the priori positions of individual galaxies, one can lower the threshold for a positive detection of their X-ray counterparts. Using a threshold of $P = 10^{-3}$, for example, we have tentatively identified another 15 faint X-ray counterparts of the radio members of the Abell 2125 complex (Owen et al. 2004a). These studies suggest that the Abell 2125 complex is in a special phase of the cluster formation, probably triggered by mergers among major components of a large-scale structure (e.g., Owen et al. 2004a). The presence of an unusually large number of active galaxies may be especially important for the heating of the IGM, affecting the subsequent evolution of the complex.

5. Summary

We have presented a deep *Chandra* ACIS-I observation of a large-scale hierarchical complex associated with the central Abell 2125 complex. The superb spatial resolution and broad energy coverage of this observation have allowed us for the first time cleanly separate contributions from discrete sources and diffuse hot gas in the complex. The

main results and conclusions we have obtained are summarized as follows:

- We have detected 99 discrete sources with an on-axis flux limit of $\sim 8 \times 10^{-16}$ erg cm $^{-2}$ s $^{-1}$ in the 0.5-8 keV band. Ten of these sources are identified to have optical counterparts spectroscopically confirmed as the complex members. X-ray sources outside the central cluster appear to be point-like and have relative hard spectral characteristics. Inside the cluster, X-ray sources/peaks are associated with giant radio galaxies and are both soft and extended, indicating an origin in diffuse hot gas. The remaining unidentified sources are statistically consistent with being interlopers.
- We have characterized the global X-ray properties of the central cluster. The ratio of the ICM temperature (3.2 keV) and the luminosity ($\sim 7.9 \times 10^{43}$ ergs s $^{-1}$ in the 0.5-2 keV band) of the central cluster appears normal. The central cluster itself is not rich, consistent with its small X-ray-inferred size. The Abell radius encloses another cluster, plus parts of other larger scale structure of the complex. The ongoing mergers in the central cluster are apparent in its morphology and kinematics. An X-ray morphology analysis shows significant intensity isophote ellipse shift with the spatial scale. An elliptical β -model gives a satisfactory fit to the surface brightness intensity profile in the 0.5-8 keV band, but not in the 0.5-2 keV band, in which morphological distortion due to substructures becomes more important.
- We confirm the detection of large amounts of low surface brightness diffuse X-ray emission in regions beyond the central cluster. In particular, the gas in the relatively prominent southwest patch has a mean thermal temperature of ~ 1 keV and a heavy element abundance of $\lesssim 9\%$ solar, substantially smaller than that in the ICM of the cluster. The diffuse X-ray emission correlates with concentrations of galaxies, most of which are spirals. This, together with the apparently low abundance, suggests that the gas represents the hot IGM associated with the large-scale

hierarchical structure formation as predicted in theories.

We thank David Smith for his help in exporting the Log(N)–Log(S) analysis into XSPEC and the referee for valuable comments. This work was funded by NASA under the grants GO1-2126 and NAG5-8999.

REFERENCES

- Arnaud, K. A. 1996, in *Astronomical Data Analysis Software and Systems V* (ASP Conf. Series volume 101), eds. Jacoby G. and Barnes J., p17
- Abell, G. O. 1958, *ApJS*, 3, 211
- Balogh, M., et al. 2002, *MNRAS*, 337, 256
- Bekki, K., Couch, W. J., & Shioya, Y. 2002, *ApJ*, 577, 651
- Brinkmann et al. 1995, *A&AS*, 109, 147
- Butcher, H. et al. 1983, *ApJS*, 52, 183
- Butcher, H., & Oemler, A., Jr. 1984, *ApJ*, 285, 426
- Dwarakanath, K. S., & Owen, F. N. 1999, *AJ*, 118, 625
- Carter, D., & Metcalfe, N. 1980, *MNRAS*, 191, 325
- Cavaliere, A., & Fusco-Femiano, R. 1976, *A&A*, 49, 137
- Cen, R., & Ostriker, J. P. 1999, *ApJ*, 514, 1
- David, L. P., Jones, C., & Forman, W. 1996, *ApJ*, 473, 692
- Edge, A. C., & Stewart, G. C. 1991, *MNRAS*, 252, 414
- Fujita, Y. 2001, *ApJ*, 550, 612
- Fukazawa, Y., Kawano, N., Ohta, A., & Mizusawa, H. 2002, *PASJ*, 54, 527
- Helsdon, S. F., & Ponman, T. J. 2002, *MNRAS*, 325, 693
- Hogg, D. W., & Turner, E. L. 1998, *PASP*, 110, 727
- Jerius, D., et al. 2000, *SPIE*, 4012, 17
- Miller et al. 2004, *ApJ*, submitted
- Moretti, A., Campana, S., Lazzati, D., & Tagliaferri, G. 2003, *A&A*, 588, 696
- Morrison, G. E., & Owen, F. N. 2003, *AJ*, 125, 506
- Owen, F. N., et al. 1999, *AJ*, 118, 633
- Owen, F. N., et al. 2004a, in preparation
- Owen, F. N., et al. 2004b, in preparation
- Ponman, T. J., et al. 1999, *Nature*, 397, 135
- Ranalli, P., Comastri, A., & Setti, G. 2003, *A&A*, 399, 39
- Roettiger, K., Burns, J., & Loken, C. 1993, *ApJL*, 407, 53
- Shimizu, M., Kitayama, T., Sasaki, S., & Suto, Y. 2003, *ApJ*, 590, 197
- Stevens, I. R., Acreman, D. M., & Ponman, T. J. 1999, *MNRAS*, 310, 663
- Tsai, J. C., & Mathews, W. G. 1996, *ApJ*, 468, 571

- Wang, Q. D., Connolly, A., & Brunner, R. 1997a, *ApJL*, 487, 13
- Wang, Q. D., Ulmer, M., & Lavery, R. J., 1997b, *MNRAS*, 292, 920
- Wang, Q. D., & Ulmer, M. 1997, *MNRAS*, 290, 920
- Wang, Q. D. 2004, in preparation
- Wang, Q. D., Chaves, T., & Irwin, J. 2003, *ApJ*, 598, 969
- West, M. J., Jones, C., & Forman, W. 1995, *ApJL*, 451, 5
- Wu, X-P., Xue, Y-J., & Fang, L-Z. 1999, *ApJ*, 524, 22

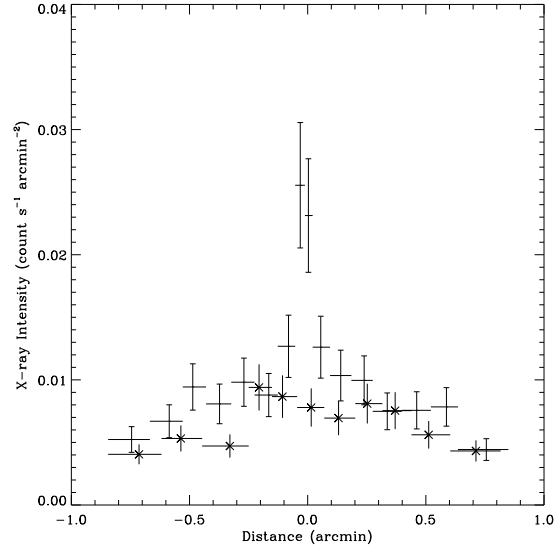


Fig. 16.— Average ACIS-I intensity distributions along a cut, which is 22" wide and perpendicular to the trail apparently following X-68 or the optical/radio galaxy C153 (see also Figs. 7c,d and 15). The data points are obtained in two bands: 0.5-1.5 keV and 1.5-4 keV (marked by "x"). The vertical error bars are at 1σ , whereas the horizontal bars represent the off-trail distance ranges of the data points.

Fig. 17.— *HST* WFPC-2 V-band images of a field near the core of the Abell 2125 cluster (a and b) and a field in the LSBXE (c and d). The overlaid X-ray intensity contours are at 2.50, 2.75, 3.25, 4.00, 5.00, 6.25, 7.75, 9.5, 14.25, 26.75, and 51.75 for the 0.5-2 keV band (a); 2.80, 3.20, 4.00, 5.20, 6.80, 8.80, 11.2, 14, 21.6, 41.6, and 81.6 for the 2-8 keV band (b); 1.55, 1.6, 1.7, 1.85, 2.05, 2.3, 2.65, 3.9, 6.4, and 11.4 for the 0.5-2 keV band (c); 2.1, 2.2, 2.4, 2.7, 3.1, 3.6, 4.3, 6.8, 11.8, and 21.8 for the 2-8 keV band (d); all in units of 10^{-3} counts s^{-1} arcmin $^{-2}$. X-ray source numbers (Table 1) are labeled.

TABLE 1
Chandra SOURCE LIST

Source (1)	CXOU Name (2)	δ_x (") (3)	log(P) (4)	CR (cts ks ⁻¹) (5)	HR (6)	HR1 (7)	HR2 (8)	Flag (9)
1	J153918.89+661700.8	2.1	-12.4	0.60 ± 0.15	—	—	—	B, H
2	J153919.36+661629.6	2.1	-13.1	0.67 ± 0.14	—	—	—	B, S
3	J153922.59+661825.4	1.0	-20.0	2.15 ± 0.21	-0.49 ± 0.13	0.51 ± 0.10	—	B, S, H
4	J153925.48+660848.2	3.1	-7.5	0.42 ± 0.12	—	—	—	S
5	J153935.02+660525.8	1.8	-20.0	1.16 ± 0.17	—	-0.09 ± 0.18	—	B, S, H
6	J153935.49+661455.9	0.7	-20.0	1.67 ± 0.17	-0.27 ± 0.14	0.50 ± 0.12	-0.69 ± 0.15	B, S, H
7	J153935.61+661244.8	1.7	-11.3	0.69 ± 0.16	—	—	—	B, S
8	J153938.08+662102.7	1.7	-15.7	1.14 ± 0.19	—	0.12 ± 0.19	—	B, S, H
9	J153945.15+660651.7	1.9	-7.2	0.78 ± 0.15	—	—	—	S
10	J153945.28+661236.1	0.5	-20.0	2.53 ± 0.28	-0.38 ± 0.14	0.29 ± 0.13	-0.55 ± 0.17	B, S, H
11	J153946.05+660702.4	1.7	-11.7	0.62 ± 0.13	—	—	—	B, H
12	J153946.67+662013.4	0.9	-15.2	2.32 ± 0.21	-0.67 ± 0.10	0.15 ± 0.10	—	B, S, H
13	J153949.30+661737.1	0.6	-20.0	2.40 ± 0.21	-0.58 ± 0.10	0.15 ± 0.10	-0.64 ± 0.17	B, S, H
14	J153952.87+660954.0	1.1	-11.9	0.43 ± 0.10	—	—	—	r, α ; B, S
15	J153957.97+661350.4	0.7	-20.0	0.84 ± 0.13	—	-0.12 ± 0.16	—	B, S
16	J153958.54+660808.5	1.6	-10.6	0.28 ± 0.09	—	—	—	S, B
17	J154000.02+660551.2	0.3	-16.1	11.72 ± 0.46	-0.40 ± 0.05	0.43 ± 0.04	-0.34 ± 0.07	B, S, H
18	J154001.51+661518.2	1.0	-10.0	0.24 ± 0.07	—	—	—	S, B
19	J154003.00+661527.1	1.1	-20.0	0.34 ± 0.08	—	—	—	B, S
20	J154003.44+661532.8	0.6	-16.7	1.12 ± 0.13	-0.42 ± 0.15	0.44 ± 0.14	—	B, S, H
21	J154005.03+661016.5	1.2	-7.1	0.24 ± 0.07	—	—	—	S
22	J154005.29+661012.5	0.9	-13.2	0.31 ± 0.08	—	—	—	r, α ; S, B
23	J154005.55+660718.5	1.3	-16.8	0.61 ± 0.11	—	—	—	B, H, S
24	J154008.12+661625.5	0.6	-17.6	0.71 ± 0.11	—	0.25 ± 0.18	—	B, S
25	J154009.13+661217.0	0.7	-15.4	0.32 ± 0.08	—	—	—	r, α ; S, B
26	J154009.20+661328.0	0.8	-15.9	0.28 ± 0.07	—	—	—	B, H
27	J154010.07+661635.2	0.6	-17.7	1.06 ± 0.13	-0.52 ± 0.15	0.11 ± 0.15	—	B, S, H
28	J154010.75+661922.5	1.1	-15.8	0.55 ± 0.10	—	—	—	B, S
29	J154012.39+661438.8	0.1	-20.0	8.57 ± 0.37	-0.52 ± 0.05	0.23 ± 0.05	-0.42 ± 0.07	B, S, H
30	J154012.55+660939.3	1.3	-9.4	0.23 ± 0.07	—	—	—	B, H
31	J154012.77+661920.3	1.2	-20.0	0.49 ± 0.10	—	—	—	B, H
32	J154014.83+661548.7	0.4	-20.0	1.38 ± 0.15	-0.52 ± 0.13	0.40 ± 0.12	—	B, S, H
33	J154016.54+661039.6	0.7	-12.4	0.27 ± 0.07	—	—	—	r, α ; B, S
34	J154017.83+661302.7	1.0	-13.0	0.27 ± 0.08	—	—	—	B, S, H
35	J154018.45+660712.6	0.7	-20.0	1.10 ± 0.14	—	-0.03 ± 0.15	—	B, S, H
36	J154023.34+661651.1	1.1	-12.4	0.26 ± 0.07	—	—	—	B, H
37	J154025.58+660838.4	0.3	-16.4	3.04 ± 0.23	-0.48 ± 0.09	0.04 ± 0.09	-0.34 ± 0.13	B, S, H
38	J154027.18+661050.6	0.4	-16.9	0.50 ± 0.09	—	0.34 ± 0.20	—	S, B
39	J154033.52+661908.4	1.0	-20.0	0.43 ± 0.09	—	—	—	B, H
40	J154033.64+660800.7	0.7	-20.0	0.60 ± 0.10	—	—	-0.20 ± 0.18	B, H, S
41	J154038.84+661125.8	0.7	-10.9	0.12 ± 0.05	—	—	—	S, B
42	J154039.11+661006.8	0.5	-20.0	0.48 ± 0.09	—	—	—	B, H, S
43	J154039.46+661713.1	0.6	-16.1	0.78 ± 0.11	—	0.61 ± 0.14	—	B, S, H
44	J154039.99+661236.6	0.2	-16.5	0.83 ± 0.11	—	0.41 ± 0.15	—	S, B, H
45	J154043.73+660844.5	0.7	-20.0	0.62 ± 0.11	—	—	—	B, S, H
46	J154044.85+660904.1	0.8	-16.1	0.68 ± 0.16	—	—	—	B, S
47	J154045.02+660507.1	1.2	-20.0	1.07 ± 0.17	—	—	—	B, S, H
48	J154045.34+661727.2	0.7	-16.0	0.38 ± 0.08	—	—	—	B, S, H
49	J154046.22+661053.3	0.8	-10.2	0.25 ± 0.09	—	—	—	B, S
50	J154046.73+661320.9	0.3	-20.0	0.30 ± 0.07	—	—	—	B, S, H
51	J154048.03+662002.9	2.0	-6.3	0.27 ± 0.08	—	—	—	B
52	J154048.55+661026.8	0.8	-7.0	0.11 ± 0.05	—	—	—	B, H
53	J154048.86+661135.4	0.3	-17.0	0.44 ± 0.09	0.86 ± 0.19	—	-0.29 ± 0.19	B, H
54	J154051.54+661414.2	0.5	-6.5	0.10 ± 0.04	—	—	—	B
55	J154052.03+660632.4	1.7	-7.0	0.28 ± 0.08	—	—	—	B, S
56	J154052.44+661236.9	0.1	-20.0	2.08 ± 0.18	-0.53 ± 0.10	0.17 ± 0.10	-0.47 ± 0.15	B, S, H
57	J154052.56+661424.9	0.5	-8.2	0.11 ± 0.04	—	—	—	S
58	J154055.69+661458.6	1.3	-6.4	0.10 ± 0.05	—	—	—	S

TABLE 1—*Continued*

Source	CXOU Name	δ_x (")	log(P)	CR (cts ks ⁻¹)	HR	HR1	HR2	Flag
(1)	(2)	(3)	(4)	(5)	(6)	(7)	(8)	(9)
59	J154056.45+661628.6	0.1	-20.0	8.80 ± 0.37	-0.54 ± 0.05	0.33 ± 0.05	-0.26 ± 0.08	B, S, H
60	J154057.13+660917.8	0.7	-12.9	0.24 ± 0.07	—	—	—	B, S
61	J154058.93+661742.6	0.9	-11.1	0.30 ± 0.08	—	—	—	B, S
62	J154059.21+660640.0	1.3	-11.6	0.36 ± 0.09	—	—	—	B
63	J154100.39+661903.0	1.5	-10.4	0.26 ± 0.08	—	—	—	r, o; S, B
64	J154102.01+661721.4	0.3	-20.0	1.79 ± 0.17	-0.54 ± 0.11	0.20 ± 0.11	-0.01 ± 0.19	o; B, S, H
65	J154102.04+661626.5	0.3	-20.0	0.73 ± 0.12	—	-0.25 ± 0.16	—	r, o; B, S
66	J154102.76+661404.7	0.2	-20.0	0.77 ± 0.11	—	0.48 ± 0.16	—	S, B, H
67	J154109.25+661448.7	0.5	-12.9	0.24 ± 0.06	—	—	—	B, S
68	J154109.79+661544.7	0.5	-8.9	0.28 ± 0.07	—	—	—	r, o; B, S
69	J154112.48+661717.0	0.9	-15.5	0.41 ± 0.09	—	—	—	B, S
70	J154112.90+660502.8	2.0	-9.6	0.32 ± 0.10	—	—	—	S, B
71	J154116.94+661627.2	0.8	-8.7	0.34 ± 0.09	—	—	—	B
72	J154117.43+661923.8	1.4	-16.2	0.43 ± 0.09	—	—	—	o; S, B
73	J154117.92+661343.0	0.4	-20.0	0.52 ± 0.09	—	—	—	B, S, H
74	J154120.83+660933.7	0.4	-16.1	1.71 ± 0.18	-0.23 ± 0.13	0.88 ± 0.07	-0.29 ± 0.16	B, S, H
75	J154121.93+661347.9	1.0	-6.3	0.12 ± 0.05	—	—	—	H
76	J154123.79+662057.2	1.5	-20.0	0.60 ± 0.12	—	—	—	B, H
77	J154127.33+661741.7	1.5	-9.8	0.39 ± 0.10	—	—	—	B, S
78	J154127.43+661413.6	0.6	-20.0	0.63 ± 0.11	—	0.79 ± 0.15	—	B, S, H
79	J154127.51+660637.6	0.8	-20.0	1.79 ± 0.18	-0.33 ± 0.14	0.38 ± 0.12	0.02 ± 0.18	B, S, H
80	J154128.35+661247.5	0.7	-12.3	0.25 ± 0.07	—	—	—	B, S
81	J154132.46+660834.5	1.1	-16.8	0.73 ± 0.14	—	0.75 ± 0.15	—	B, S
82	J154133.15+661215.8	0.9	-13.5	0.30 ± 0.08	—	—	—	S, B
83	J154133.78+661341.8	0.8	-16.2	0.40 ± 0.08	—	—	—	B, S
84	J154133.86+660728.6	1.3	-14.0	0.44 ± 0.10	—	—	—	B, S
85	J154137.33+661506.7	1.1	-8.5	0.28 ± 0.08	—	—	—	B, S
86	J154141.29+660531.0	1.5	-20.0	0.95 ± 0.15	—	0.35 ± 0.17	—	B, S
87	J154143.47+661419.4	1.0	-14.0	0.31 ± 0.08	—	—	—	r, o; B, S
88	J154144.13+661848.7	1.3	-13.9	0.48 ± 0.10	—	0.83 ± 0.16	—	B, S
89	J154144.72+661143.0	1.6	-8.6	0.26 ± 0.07	—	—	—	B, S
90	J154145.99+661038.3	1.6	-8.9	0.28 ± 0.08	—	—	—	B, S
91	J154156.70+660738.9	1.9	-10.7	0.51 ± 0.12	—	—	—	B, S
92	J154157.12+661211.6	0.5	-17.5	2.38 ± 0.20	-0.09 ± 0.11	0.86 ± 0.07	-0.31 ± 0.12	B, S, H
93	J154158.26+661312.5	1.1	-15.9	0.66 ± 0.14	—	—	—	B, S
94	J154159.60+661514.9	1.4	-12.2	0.38 ± 0.09	—	—	—	B, S
95	J154200.02+661843.8	2.0	-10.5	0.52 ± 0.11	—	—	—	B, H
96	J154200.21+661053.0	1.8	-7.2	0.30 ± 0.09	—	—	—	B, H
97	J154205.44+661604.4	1.0	-20.0	1.15 ± 0.15	0.68 ± 0.13	—	-0.46 ± 0.13	B, H, S
98	J154205.78+661529.1	1.9	-9.6	0.43 ± 0.11	—	—	—	B, H
99	J154205.82+661629.8	1.6	-16.5	0.69 ± 0.15	—	0.53 ± 0.20	—	S, B

NOTE.—Column (1): Generic source number. (2): *Chandra* X-ray Observatory (unregistered) source name, following the *Chandra* naming convention and the IAU Recommendation for Nomenclature (e.g., <http://cdsweb.u-strasbg.fr/iau-spec.html>). (3): Position uncertainty (1σ) in units of arcsec. (4): The false detection probability P that the detected number of counts may result from the Poisson fluctuation of the local background within the detection aperture [$\log(P)$ smaller than -20.0 is set to -20.0]. (5): On-axis (exposure-corrected) source count rate in the 0.5–8 keV band. (6–8): The hardness ratios defined as $HR = (H - S)/(H + S)$, $HR1 = (S2 - S1)/S$, and $HR2 = (H2 - H1)/H$, where S1, S2, H1, and H2 are the net source count rates in the 0.5–1, 1–2, 2–4, and 4–8 keV bands, respectively, while S and H represent the sums, $S1+S2$ and $H1+H2$. The hardness ratios are calculated only for sources with individual signal-to-noise ratios greater than 4 in the broad band ($B=S+H$), and only the values with uncertainties less than 0.2 are included. (9): The label “B”, “S”, or “H” mark the band in which a source is detected; the detection with the most accurate position, as adopted in Column (2), is marked first. The label “r” and “o” denote the identification as the Abell 2125 complex member galaxies in radio and optical.

TABLE 2
RESULTS OF SPECTRAL FITS

Parameter	Cluster	LSBXE
Best-fit $\chi^2/\text{d.o.f.}$	155/151	22/25
Column Density (10^{20} cm^{-2})	1.6($\lesssim 3.7$)	0.1 ($\lesssim 10$)
Abundance (10^{-2} solar)	0.24(0.12-0.39)	0.03($\lesssim 0.09$)
Temperature (keV)	3.2(2.8-3.7)	0.98(0.71-1.2)
Integrated EM (10^{10} cm^{-5})	5.8(5.3-6.4)	4.0(3.1-7.6)
$L_{0.5-8\text{keV}}$ ($10^{43} \text{ erg s}^{-1}$)	7.9	2.0

NOTE.—The uncertainty ranges of the parameters are included in the parentheses and are all at the 90% confidence. The integrated emission measure is defined as $1/4\pi \int_{\Omega} \text{EM} d\Omega$, where the integration is over a solid angle over which the data are collected and $\text{EM} = \int n_e^2 dr$ with n_e being the electron density (all units in cgs).

TABLE 3
 β -MODEL FITS TO THE CLUSTER SURFACE BRIGHTNESS PROFILES

Parameter	0.5-8 keV band	0.5-2 keV band
Center R.A. (J2000)	15 ^h 41 ^m 11 ^s .3	15 ^h 41 ^m 11 ^s .6
Center Dec. (J2000)	66°16'2"	66°16'3"
Ellipticity	0.29	0.29
Position angle (°)	123	120
β	0.52 (0.47-0.58)	0.62 (0.56-0.73)
r_c (')	0.910 (0.773-1.08)	1.20(1.04-1.46)
(kpc)	210(178 - 248)	276 (240-336)
$I_o(10^{-2} \text{ cts s}^{-1} \text{ arcmin}^{-2})$	2.1(1.9-2.2)	1.5(1.3-1.6)
$\chi^2/\text{d.o.f.}$	66/56	96/56

NOTE.—Uncertainties in parameter values, as presented in parentheses, are all at the 90% confidence level.

This figure "f1.jpeg" is available in "jpeg" format from:

<http://arxiv.org/ps/astro-ph/0404602v1>

This figure "f2a.jpeg" is available in "jpeg" format from:

<http://arxiv.org/ps/astro-ph/0404602v1>

This figure "f2b.jpeg" is available in "jpeg" format from:

<http://arxiv.org/ps/astro-ph/0404602v1>

This figure "f7.png" is available in "png" format from:

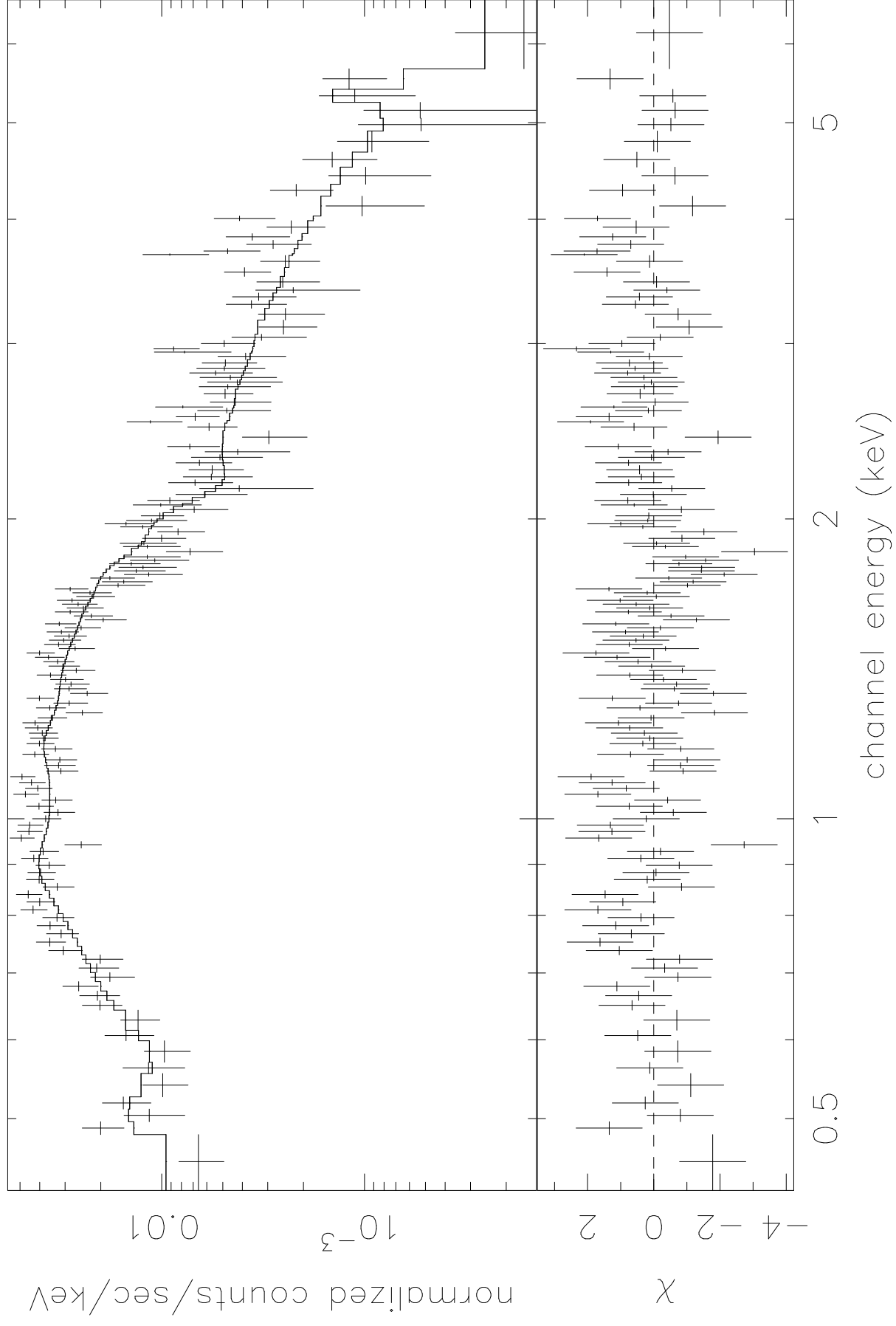
<http://arxiv.org/ps/astro-ph/0404602v1>

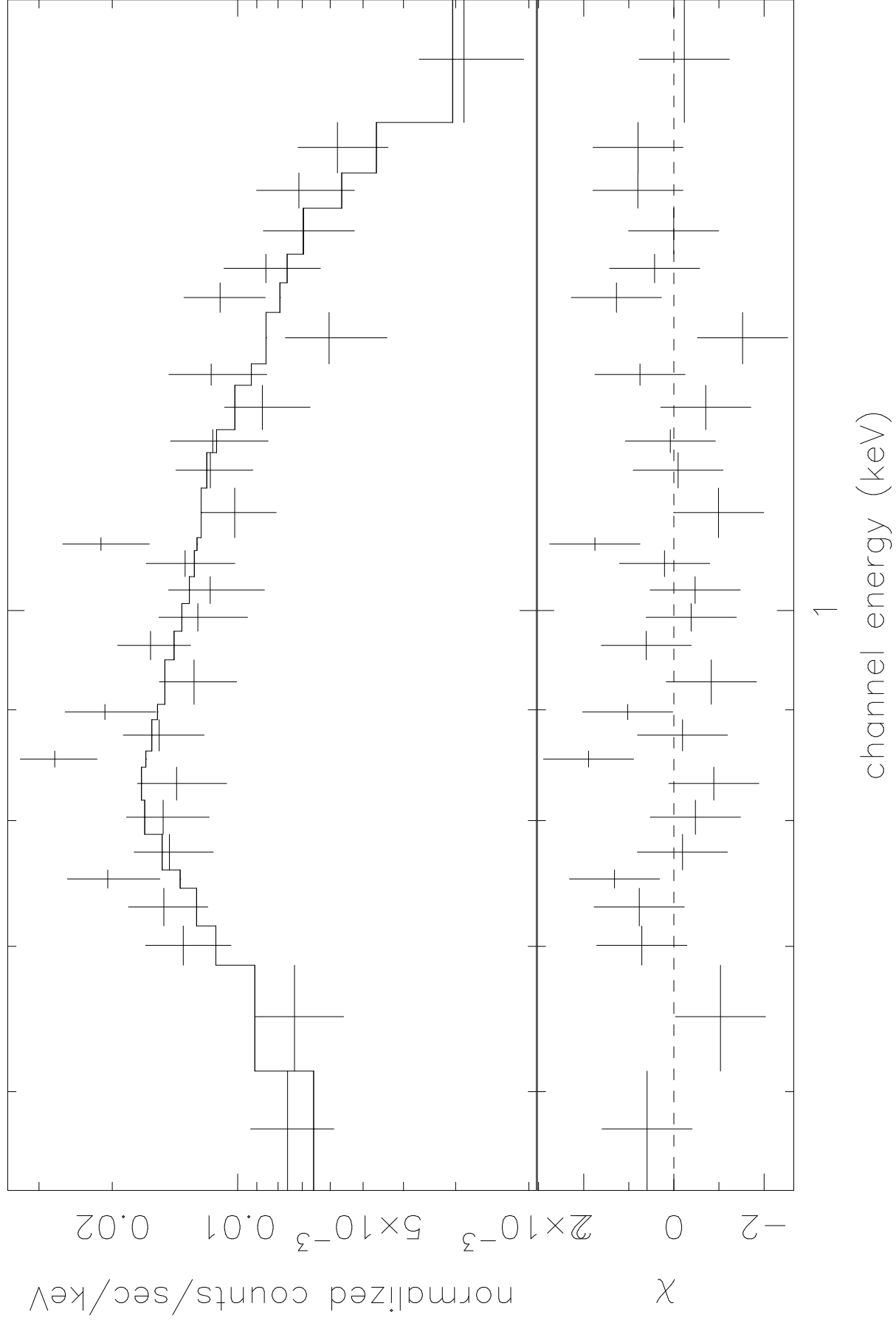
This figure "f8.png" is available in "png" format from:

<http://arxiv.org/ps/astro-ph/0404602v1>

This figure "f9.png" is available in "png" format from:

<http://arxiv.org/ps/astro-ph/0404602v1>





This figure "f12.png" is available in "png" format from:

<http://arxiv.org/ps/astro-ph/0404602v1>

This figure "f15.png" is available in "png" format from:

<http://arxiv.org/ps/astro-ph/0404602v1>

This figure "f17.png" is available in "png" format from:

<http://arxiv.org/ps/astro-ph/0404602v1>